

Eddy-viscosity-improved resolvent analysis of compressible turbulent boundary layers

Yitong Fan^{1,2}, Melissa Kozul², Weipeng Li^{1,†} and Richard D. Sandberg²

¹School of Aeronautics and Astronautics, Shanghai Jiao Tong University, Shanghai 200240, PR China

²Department of Mechanical Engineering, University of Melbourne, Parkville, VIC 3010, Australia

(Received 31 October 2023; revised 3 February 2024; accepted 17 February 2024)

An improved resolvent analysis is proposed in the regime of compressible turbulent boundary layers. To better model nonlinear processes in the input, the resolvent framework is augmented by adding eddy viscosity. To this end, we propose two eddy-viscosity models: a modified Cess eddy-viscosity model coupling the compressibility transformation and outer-layer correction, and a new eddy-viscosity model based on an empirical relationship and mixing-length theory. Both are incorporated into the resolvent operator to examine the performance of the eddy-viscosity-improved resolvent-based reduced-order modelling. Results of the augmented resolvent analysis are compared qualitatively and quantitatively with the first leading mode of spectral proper orthogonal decomposition, by checking the profiles and cross-spectral densities of velocities, density and temperature in two hypersonic turbulent boundary layers under different wall conditions. Higher accuracy of the turbulence prediction is achieved by adding the proposed eddy-viscosity models, particularly for the energetic cycle in the outer-layer region where strong nonlinear energy transfer exists.

Key words: turbulence modelling, turbulent boundary layers, compressible turbulence

1. Introduction

Resolvent analysis is known as a promising operator-theoretic modal decomposition method in fluid dynamics (McKeon & Sharma 2010; Taira *et al.* 2017; Jovanović 2021). Based on linear dynamical system theory, the Navier–Stokes equations are linearized around the steady base flow to form an input–output framework, governed by the resolvent operator. Resolvent analysis has been used widely to identify the prominent linear mechanisms, predict the organization of coherent structures, and design optimal flow-control algorithms, for canonical wall-bounded turbulence (Sharma & McKeon 2013; Zare, Jovanović & Georgiou 2017; Martini *et al.* 2020, 2022; Karban *et al.* 2022), mixing

† Email address for correspondence: liweipeng@sjtu.edu.cn

jets (Schmidt *et al.* 2018; Towne, Schmidt & Colonius 2018; Lesshafft *et al.* 2019; Pickering *et al.* 2021), bluff-body wakes (Jin, Symon & Illingworth 2021; Jin, Illingworth & Sandberg 2022) and shock buffet (He & Timme 2020; Kojima *et al.* 2020), to name a few.

Performing singular value decomposition of the resolvent operator, the response to the endogenous stimulus is ranked at particular wavenumber and frequency pairs. By selecting the optimal response modes, the chaotic motions in wall-bounded turbulence can be characterized by the low-rank approximation of resolvent modes. For instance, Sharma & McKeon (2013) identified the complex coherent structures in turbulent pipe flow, based on a single optimal response mode or a linear superposition of modes at representative wavenumber combinations. Moarref *et al.* (2013*a*) exploited the optimal resolvent modes as basis functions to predict streamwise velocity fluctuations in high-Reynolds-number channel flows. A convex optimization problem was solved to determine the weight functions amplifying or attenuating the energy densities of the optimal modes, and good agreements with experimental or well-resolved numerical results were achieved. Similar optimization algorithms were also applied to estimate the distribution of spanwise and wall-normal velocity fluctuations, and the Reynolds shear stress across the wall layer (Moarref *et al.* 2013*b*, 2014). Abreu *et al.* (2020) used the resolvent analysis and spectral proper orthogonal decomposition (SPOD) to identify the dominant near-wall coherent structures in channel flows. Quantitative comparisons suggested that the resolvent and SPOD modes are consistent with each other, especially at the frequencies and wavenumbers where the lift-up mechanism is present. In the context of compressible wall turbulence, Dawson, McKeon & Saxton-Fox (2018) and Dawson & McKeon (2019) extended the resolvent formulation to a compressible form, by incorporating the advection–diffusion equation of temperature (or any scalar), allowing the prediction of passive scalar structures. Compressible resolvent analysis has been applied to supersonic/hypersonic wall-bounded turbulence, for various purposes, including revealing the features of energy-distribution mechanisms and examining the scaling laws of resolvent modes (Bae, Dawson & McKeon 2020*a,b*), identifying coherent structures under the condition of wall cooling (Fan, Li & Sandberg 2023), and analysing the mechanisms responsible for the energy amplification in subsonic and supersonic response modes (Madhusudanan & McKeon 2022; Chen *et al.* 2023).

Recently, various modifications to the standard resolvent formulation have been proposed to improve the accuracy of resolvent-based modelling and prediction (McKeon 2017; Gupta *et al.* 2021; Wu & He 2023). Among the modifications, a critical point is that the nonlinear process in the resolvent formulation needs to be modelled appropriately. Generally, a stochastic excitation is imposed on the linear system as an input, to avoid the calculation or modelling of the complex nonlinear terms. However, this strategy may lead to a poor performance of prediction. For instance, Symon, Illingworth & Marusic (2021) reported that given white noise inputs, the predicted production term in the turbulent kinetic energy budgets is much larger than the inter-scale transfer term, which conflicts with the real physics. They found that this unphysical phenomenon is associated directly with the non-normality in the resolvent operator, and it can be alleviated by adding appropriate eddy viscosity to the resolvent formulation, so as to account for part of the nonlinear process. In the resolvent analysis of incompressible turbulent channel flows, the Cess eddy-viscosity model (Cess 1958; Reynolds & Hussain 1972) is used widely. Significant improvements of accuracy were achieved, for the prediction of instantaneous velocity fields (Illingworth, Monty & Marusic 2018; Madhusudanan, Illingworth & Marusic 2019), energy transfer (Symon *et al.* 2021) and spatio-temporal

power spectral densities (Morra *et al.* 2019, 2021; Symon, Illingworth & Marusic 2020), especially for the high-energy-containing scales. The turbulent dissipation introduced by the eddy viscosity plays an important role in modelling the nonlinear transfer from large- to small-scale motions (Symon *et al.* 2021, 2023). Aiming to model the remaining part of the nonlinear process, Gupta *et al.* (2021) decomposed the nonlinear terms into two parts, the eddy-viscosity term and the improved stochastic-forcing term. The two terms were modelled separately as functions of the wall distance and turbulence scales, to estimate the large-scale fluctuations at different wall-normal locations in channel flows.

So far, no eddy-viscosity model has been developed for the resolvent analysis in the case of compressible turbulent boundary layers, to the best of the authors' knowledge. Due to the different geometries between the channel and boundary layer, the classical Cess model, without modifications, may not be suitable for turbulent boundary layers, especially for the dynamics in the outer region. On the other hand, in compressible turbulent boundary layers, the mean velocity profiles differ from their incompressible counterparts due to the variations of thermodynamic properties. The Cess eddy-viscosity model (Cess 1958; Reynolds & Hussain 1972) is defined such that the universal mean velocity profile in incompressible channel flows is obtained by simply integrating the expression $Re_\tau(1 - x_2)\mu_w/\mu_T$ in the wall-normal direction. (In this expression, Re_τ is the friction Reynolds number, μ_w and μ_T are the wall dynamic and total viscosities, and x_2 is the normalized wall-normal distance to the surface.) However, with rapid density variations in the compressible cases, the velocity profiles deviate from those resulting from the classical Cess model. Therefore, compressibility effects need to be taken into account in the development of eddy-viscosity models for compressible flows.

In the present study, two eddy-viscosity models are proposed to improve the resolvent analysis for compressible turbulent boundary layers: (i) the classical Cess eddy-viscosity model is modified by coupling a compressibility transformation with an outer-layer correction; (ii) we develop a new eddy-viscosity model based on an empirical expression and the mixing-length theory. To examine their capability in resolvent-based modelling, we apply them to the resolvent formulation for two hypersonic turbulent boundary layers under different wall conditions. The remainder of the paper is outlined as follows. Section 2 introduces the resolvent formulation for the compressible turbulent boundary layers, with/without the addition of eddy viscosity. Two eddy-viscosity models are proposed herein, with *a priori* examinations conducted in contrast to the direct numerical simulations (DNS) data. In § 3, to evaluate the performance of eddy-viscosity-improved resolvent-based reduced modelling, we compare the predicted perturbations in velocities, density and temperature to those issued from the SPOD. Finally, concluding remarks are given in § 4.

2. Methodology

2.1. Governing equations

For a perfect heat-conduction gas, the non-dimensional compressible Navier–Stokes equations are given as

$$\rho \left(\frac{\partial u_i}{\partial t} + u_j \frac{\partial u_i}{\partial x_j} \right) = -\frac{1}{\gamma M_\infty^2} \frac{\partial p}{\partial x_i} + \frac{1}{Re} \frac{\partial}{\partial x_j} \left[\mu \left(\frac{\partial u_i}{\partial x_j} + \frac{\partial u_j}{\partial x_i} \right) + \lambda \frac{\partial u_k}{\partial x_k} \delta_{ij} \right], \quad (2.1)$$

$$\frac{\partial \rho}{\partial t} + u_j \frac{\partial \rho}{\partial x_j} = -\rho \frac{\partial u_j}{\partial x_j}, \quad (2.2)$$

$$\rho \left(\frac{\partial T}{\partial t} + u_j \frac{\partial T}{\partial x_j} \right) = -(\gamma - 1)p \frac{\partial u_i}{\partial x_i} + \frac{\gamma}{Re} \frac{\partial}{\partial x_j} \left(k \frac{\partial T}{\partial x_j} \right) + \gamma(\gamma - 1) \frac{M_\infty^2}{Re} \left[\mu \frac{\partial u_i}{\partial x_j} \frac{\partial u_i}{\partial x_j} + \mu \frac{\partial u_i}{\partial x_j} \frac{\partial u_j}{\partial x_i} + \lambda \left(\frac{\partial u_k}{\partial x_k} \right)^2 \right], \quad (2.3)$$

where t is time, x_k ($k = 1, 2, 3$) denote the streamwise, wall-normal and spanwise directions, respectively, and u_k are the corresponding velocity components. Here, ρ is density, p is pressure, and T is temperature, and they satisfy the ideal gas state equation $p = \rho T$. Also, μ and $\lambda = -2/3\mu$ are the coefficients of the molecular and second viscosity, respectively. The heat conduction coefficient k is defined by μ/Pr , where Pr is the molecular Prandtl number. Also, γ is the specific heat ratio, δ_{ij} is the Kronecker delta, and M_∞ is the freestream Mach number. The freestream Reynolds number Re is defined by $\rho_\infty^* u_\infty^* \delta_{99}^*/\mu_\infty^*$, with δ_{99} being the 99 % boundary-layer thickness. The subscript ∞ denotes the freestream state, and the superscript $*$ denotes dimensional values, otherwise all variables are non-dimensionalized by the freestream flow quantities.

2.2. Resolvent analysis

The boundary-layer flow is assumed to be locally parallel (Bae *et al.* 2020a), that is, the effects of streamwise development are ignored. Thus flow quantities $\mathbf{q} = [u_1, u_2, u_3, \rho, T]^T$ can be Fourier transformed in the temporal, streamwise and spanwise directions, namely

$$\mathbf{q}(x_1, x_2, x_3, t) = \iiint_{-\infty}^{\infty} \hat{\mathbf{q}}(x_2; \kappa_1, \kappa_3, \omega) \exp(i(\kappa_1 x_1 + \kappa_3 x_3 - \omega t)) d\kappa_1 d\kappa_3 d\omega, \quad (2.4)$$

where $\widehat{(\cdot)}$ denotes the Fourier-transformed variable, κ_1 and κ_3 are the streamwise and spanwise wavenumbers, ω is the temporal frequency, and $i = \sqrt{-1}$. The speed of the streamwise wave is defined by $c = \omega/k_x$.

Substituting (2.4) into the non-dimensional compressible Navier–Stokes equations (2.1)–(2.3), we get a linearized form for each $(\kappa_1, \kappa_3, \omega) \neq (0, 0, 0)$ (Mack 1984),

$$[-i\omega \mathbf{I} + \mathbf{L}(\kappa_1, \kappa_3, \omega)] \hat{\mathbf{q}}(x_2; \kappa_1, \kappa_3, \omega) = \hat{\mathbf{f}}(x_2; \kappa_1, \kappa_3, \omega), \quad (2.5)$$

where \mathbf{I} is the identity matrix. The high-order nonlinear contributions in the Navier–Stokes equations are all represented within a single forcing term $\hat{\mathbf{f}}$. For the detailed expression of \mathbf{L} , readers can refer to Fan *et al.* (2023).

Equation (2.5) leads to an input–output form

$$\hat{\mathbf{q}}(x_2; \kappa_1, \kappa_3, \omega) = \mathbf{H}(\kappa_1, \kappa_3, \omega) \hat{\mathbf{f}}(x_2; \kappa_1, \kappa_3, \omega), \quad (2.6)$$

where $\mathbf{H}(\kappa_1, \kappa_3, \omega) = (-i\omega \mathbf{I} + \mathbf{L}(\kappa_1, \kappa_3, \omega))^{-1}$ is termed the resolvent operator, which linearly relates the input forcing to the output state. To characterize the resolvent operator \mathbf{H} , a singular value decomposition is used, with a weight matrix taken into account for a physically appropriate norm for compressible turbulent boundary layers, that is,

$$\mathbf{W}^{1/2} \mathbf{H} \mathbf{W}^{-1/2} = \sum_{p=1}^N \tilde{\boldsymbol{\psi}}_p \sigma_p \tilde{\boldsymbol{\phi}}_p^\dagger, \quad \boldsymbol{\phi}_p = \mathbf{W}^{-1/2} \tilde{\boldsymbol{\phi}}_p, \quad \boldsymbol{\psi}_p = \mathbf{W}^{-1/2} \tilde{\boldsymbol{\psi}}_p, \quad (2.7a-c)$$

where N is the number of resolvent modes, $\boldsymbol{\psi}_p$ and $\boldsymbol{\phi}_p$ are the p th orthogonal basis functions of the response and forcing modes, and the real singular value σ_p represents

the linear amplification rate ranked by $\sigma_p > \sigma_{p+1}$. The weight matrix selected here is defined by Chu (1965), i.e. $\mathbf{W} = \text{diag}(\bar{\rho}, \bar{\rho}, \bar{\rho}, \bar{T}/\gamma M^2 \bar{\rho}, \bar{\rho}/\gamma(\gamma - 1)M^2 \bar{T}) dx_2$, where the overline represents Reynolds averaging. In such a way, the corresponding norm $\langle \hat{q}, \hat{q} \rangle = \hat{q}^\dagger \mathbf{W} \hat{q}$ (where the superscript \dagger denotes the complex conjugate transpose) eliminates the pressure-related energy transfer terms (compression work) and has been used widely in studies of compressible flows.

2.3. Improved resolvent analysis with addition of eddy viscosity

To model part of the pivotal nonlinear contribution, a widely acknowledged method is to add an eddy-viscosity term in the linearized Navier–Stokes equations. The role of the eddy viscosity is to introduce a closure, establishing a constitutive relation between the oscillation of Reynolds stresses associated with the passage of the disturbance and the strain rate of the turbulent motions (Illingworth *et al.* 2018; Symon *et al.* 2021; Holford, Lee & Hwang 2023). The same approach is applied to the relation between the fluctuations of turbulent heat flux and the temperature gradient in the energy equation. In this way, a new set of non-dimensional linearized Navier–Stokes equations is obtained:

$$\begin{aligned} \hat{q}(x_2; \kappa_1, \kappa_3, \omega) &= \mathbf{H}_e(\kappa_1, \kappa_3, \omega) \hat{f}(x_2; \kappa_1, \kappa_3, \omega) \\ &= (-i\omega \mathbf{I} + \mathbf{L}_e(\kappa_1, \kappa_3, \omega))^{-1} \hat{f}(x_2; \kappa_1, \kappa_3, \omega). \end{aligned} \quad (2.8)$$

In the eddy-embedded resolvent operator \mathbf{H}_e , substitutions are made for the momentum and energy equations, that is,

$$\mu \rightarrow \mu + \mu_t, \quad \lambda \rightarrow \lambda + \lambda_t \quad \text{and} \quad k \rightarrow k + k_t = \frac{\mu}{Pr} + \frac{\mu_t}{Pr_t}, \quad (2.9a-c)$$

where μ_t and λ_t are the eddy molecular and second viscosity coefficients, respectively. Here, Pr_t is the turbulent Prandtl number, which is nearly constant in most regions of the boundary layer and is mostly insensitive to the freestream Mach number and wall temperature conditions (Zhang, Duan & Choudhari 2018). In this study, we set Pr_t to 0.85, which is informed by previous studies (Zhang *et al.* 2014), and our preliminary tests showed that this value does not influence the prediction results, which was also reported by Chen *et al.* (2023). As the additional part compensates for the inter-scale energy transfer in the physical process, the resolvent operator \mathbf{H}_e is able to provide a more promising tool for prediction than \mathbf{H} . Accordingly, this eddy-viscosity-improved resolvent operator can also be characterized by singular value decomposition, leading to the response and forcing modes as $\psi_{e,p}$ and $\phi_{e,p}$. The definition of the norm $\langle \hat{q}, \hat{q} \rangle = \hat{q}^\dagger \mathbf{W} \hat{q}$ given by Chu (1965) is used here, yielding an energy eliminating the pressure-related work.

2.3.1. A modified Cess eddy-viscosity model

An issue here is how to define the profile of eddy viscosity (μ_t) in the compressible boundary layer. In resolvent analysis of incompressible channel flows, the Cess approximation has been used commonly and proved to be efficient in recovering the energetic modes. As is derived from the mean momentum equation for incompressible

channel flows, this algebraic total-viscosity model (Cess 1958) is given as

$$\frac{\mu_{T,Cess}}{\mu_w} = \frac{1}{2} \left(1 + \frac{\kappa^2 Re_\tau^2}{9} (2x_2 - x_2^2)^2 (3 - 4x_2 + 2x_2^2)^2 \left[1 - \exp\left(\frac{-Re_\tau x_2}{A}\right) \right]^2 \right)^{1/2} + \frac{1}{2}, \tag{2.10}$$

where $\kappa = 0.426$ and $A = 25.4$, following previous studies (Pujals *et al.* 2009; Amaral *et al.* 2021). The subscript w denotes quantities at the wall.

However, in the case of compressible turbulent boundary layers, the situation differs (see the Introduction). The turbulent boundary layer is a composite layer, which can be characterized by two regions associated with different fluid responses to shear and pressure gradient (Cebeci 1971). Therefore, in the present study, we decompose the boundary layer into two separate regions, i.e. the inner and outer regions, where different strategies of modelling are developed. Note that the so-called ‘inner’ and ‘outer’ regions in the remainder of the paper are here used as broad concepts, distinguishing the regions nearer the wall ($x_2 \leq \delta_c$) and further away from the wall ($x_2 > \delta_c$), where δ_c is the crossover wall-normal position. This differs from the classical identification of layers related to the mean-velocity behaviour.

In the inner region, we adopt the Cess approximation, considering that the dynamics there is very similar to that in channel flows (Pope 2000), whereas in the outer region, since the boundary-layer flow behaviour departs from that in channels, the Cess model (2.10), which is specifically derived for incompressible channel flows, is not applicable. Moreover, the Cess formulation does not consider the region outside the boundary-layer thickness. In this sense, we propose to define the eddy viscosity based on Prandtl’s mixing-length hypothesis in the outer region. Consequently, a two-layer algebraic eddy-viscosity model is proposed, generalizing the Cess model to the regime of compressible turbulent boundary layers:

$$\mu_t = \begin{cases} \sqrt{\frac{\bar{\rho}}{\rho_w}} \mu_{T,Cess} - \bar{\mu}, & \text{for } x_2 \leq \delta_c, \\ Re \bar{\rho} l_m^2 \left| \frac{d\bar{u}_1}{dx_2} \right|, & \text{for } x_2 > \delta_c, \end{cases} \tag{2.11}$$

where l_m is the mixing length (Pope 2000).

In the modified model (2.11), when $x_2 \leq \delta_c$, the original Cess total-viscosity definition is premultiplied by $\sqrt{\bar{\rho}/\rho_w}$, so that the velocity profile obtained from the integral of $Re_\tau (1 - x_2)\mu_w/\mu_T$ still follows the classical velocity laws, upon van Driest transformation (van Driest 1951) (especially suitable for the adiabatic cases). The subscript T denotes the total quantity, which means $\mu_T = \mu_t + \bar{\mu}$, with the first term representing the turbulent contribution, and the second the mean molecular viscosity. When $x_2 > \delta_c$, the eddy viscosity is determined by Prandtl’s mixing-length hypothesis. It is necessary to specify the expression of l_m that we are concerned about. Normally, it can be approximated as a constant in the outer region (core region) (Cebeci 2004). For example, Escudier (1966) set l_m to be the minimum value of κx_2 (which is assumed to be the l_m expression in the logarithmic region) in the core region and 0.09. In the present study, to ensure the continuity of the μ_t profile across the boundary layer, l_m is determined so that the μ_t at $x_2 = \delta_c$ calculated from the first and second parts of (2.11) are equal. This treatment

is believed to be reasonable, and the following results suggest that it yields a good approximation of turbulent eddy viscosity in the outer region.

2.3.2. A new semi-empirical eddy-viscosity model

We propose another approach to estimate the eddy-viscosity profile, based on an empirical law and the mixing-length theory, which is especially suitable for zero-pressure-gradient turbulent boundary layers. It is still a two-layer eddy-viscosity model, with major differences from (2.11) in the inner region. Instead of a Cess-based correction originated from the channel-flow models, here we start from the universal scaling of the total shear stress, which is exclusive for turbulent boundary layers and hence will potentially lead to a more accurate eddy-viscosity profile.

In zero-pressure-gradient turbulent boundary layers, Hou, Somandepalli & Mungal (2006) found that the $(1 - x_2)$ weighted total shear stress (τ) can be fitted by a linear expression in the region $x_2 \leq 0.5$. This $(1 - x_2)$ fit is expressed as

$$(1 - x_2) \frac{\tau}{\tau_w} = ax_2 + b, \quad \text{for } x_2 \leq 0.5, \quad (2.12)$$

where τ_w is the wall shear stress. The intercept b is fixed as $b = 1$ to ensure $\tau = \tau_w$ at $x_2 = 0$. The slope $-a$ lies in the range from 1.2 to 1.6 (Hou *et al.* 2006). The databases of numerical and experimental results for a wide range of Reynolds numbers suggested that there is no clear dependence of $-a$ on the Reynolds number (Hou *et al.* 2006; Xia, Zhang & Yang 2021).

To examine the feasibility of (2.12) for compressible turbulent boundary layers, the profiles of the weighted total shear stress at various Mach numbers and Reynolds numbers are depicted in figure 1. Details of the cases at the freestream Mach number $M = 2, 3, 4$ with the friction Reynolds number Re_τ ranging from 250 to 1110 can be retrieved from Pirozzoli & Bernardini (2011) and Bernardini & Pirozzoli (2011). The hypersonic databases at $M = 5.86$, $Re_\tau \approx 420$ and the wall-to-recovery temperature ratios $T_w/T_r = 1.0$ and 0.25, representing the adiabatic and cold-wall conditions, are obtained from DNS in Fan, Li & Pirozzoli (2022) and Fan & Li (2023). In figure 1, good alignment is observed between the weighted total shear stress and the fitting law $-1.3x_2 + 1$ in $x_2 \leq 0.5$, for all of the compressible cases considered, confirming its suitability for the empirical modelling.

In the region further away from the wall ($x_2 > \delta_c$), mixing-length theory is also exploited, leading to the analytical description of the new eddy-viscosity profile across the boundary layer:

$$\mu_t = \begin{cases} \frac{\mu_w}{d\bar{u}_1^+/d\bar{x}_2^+} \frac{-1.3x_2 + 1}{1 - x_2} - \bar{\mu}, & \text{for } x_2 \leq \delta_c, \\ Re \bar{\rho} l_m^2 \left| \frac{d\bar{u}_1}{dx_2} \right|, & \text{for } x_2 > \delta_c, \end{cases} \quad (2.13)$$

where the superscript $+$ denotes normalization by wall units. To ensure the applicability of the model in $x_2 \leq \delta_c$, δ_c should not be larger than 0.5. On the other hand, a crossover position too close to the wall is also avoided under the constant- l_m assumption. Conservatively, we make $\delta_c = 0.5$ for the cases under scrutiny in the following study.

2.3.3. A priori comparison with DNS results

Hereafter, we focus on hypersonic turbulent boundary layers at $M = 5.86$ with adiabatic and cold-wall conditions, since the compressibility effects in these cases are strong and,

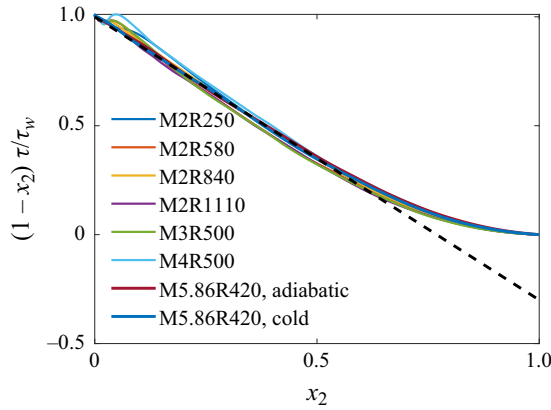


Figure 1. The DNS profiles of $(1 - x_2)\tau/\tau_w$ in compressible zero-pressure-gradient turbulent boundary layers, at: $M = 2$, $Re_\tau \approx 250$ –1110 (Pirozzoli & Bernardini 2011); $M = 3$, $Re_\tau \approx 500$ and $M = 4$, $Re_\tau \approx 500$ (Bernardini & Pirozzoli 2011); and $M = 5.86$, $Re_\tau \approx 420$ under the adiabatic and cold-wall conditions (Fan *et al.* 2022; Fan & Li 2023). The black dashed line denotes the linear expression $-1.3x_2 + 1$.

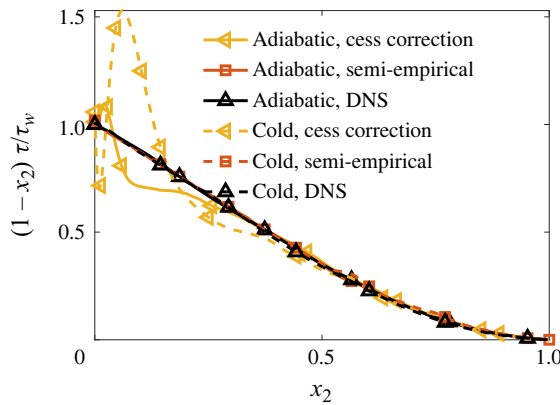


Figure 2. Modelled profiles of $(1 - x_2)\tau/\tau_w$ in the adiabatic and cold-wall hypersonic turbulent boundary layer at $M = 5.86$.

more importantly, we have detailed DNS solutions to evaluate the performance of the resolvent-based modelling. With the models (2.11) and (2.13), the distribution of the total shear stress across the boundary layer can be obtained on the basis of known mean flow quantities (a requirement for resolvent analysis), including the velocities, density and temperature. Figure 2 compares the modelled weighted total shear stress $((1 - x_2)\tau/\tau_w = (1 - x_2)(\mu_t + \bar{\mu})(d\bar{u}_1/dx_2)/\tau_w)$ with the DNS results. The total stresses predicted with the semi-empirical model are found to collapse perfectly onto the DNS profiles, whereas with the Cess-correction model, there are obvious deviations, especially in the inner region.

Figure 3 quantifies the total viscosity (μ_T/μ_w) profile across the boundary layer. It can be seen that both models proposed here capture the trends of the DNS profiles. Note that the eddy viscosity in DNS is solved from the Reynolds stress expressions based on the turbulent viscosity hypothesis. Nonetheless, the semi-empirical eddy-viscosity model is more accurate, with the profiles almost collapsed onto those of the DNS, according to the

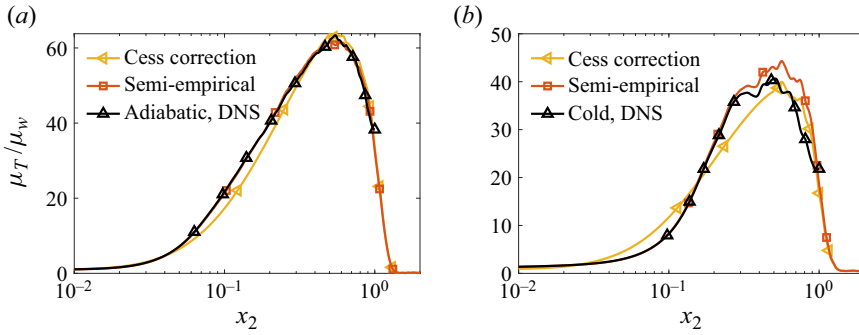


Figure 3. Profiles of the total viscosity μ_T/μ_w in the (a) adiabatic and (b) cold-wall hypersonic turbulent boundary layer at $M = 5.86$.

a priori examinations. In the next section, both eddy-viscosity models will be utilized in the resolvent operator, to examine their roles in the performance of resolvent-based flow modelling.

3. Consistency between the resolvent modes and SPOD modes

Spectral proper orthogonal decomposition (Lumley 1967; Berkooz, Holmes & Lumley 1993; Towne *et al.* 2018) is known as a promising data-driven tool to construct a reduced-order model of fluctuating flow fields, from the perspective of energy. It extracts the orthogonal basis functions at discrete frequencies from a series of snapshots using Welch’s method, with the leading SPOD modes to be optimally representative of the turbulent energy of the system (Taira *et al.* 2017; Towne *et al.* 2018). This section aims to examine the similarity between the SPOD modes issued from the DNS data and the response modes from the resolvent analysis with/without eddy viscosity, to evaluate the feasibility of resolvent-based reduced-order modelling (Abreu *et al.* 2020; Pickering *et al.* 2021) in the compressible regime.

Figure 4 quantifies the energy ratios of the first eight leading resolvent and SPOD modes, at two representative scales in the adiabatic and cold-wall turbulent boundary layers. The scales are selected at positions of local energy peaks characterizing the inner- and outer-layer dynamics, referring to our previous study (Fan & Li 2023). It is observed that the first mode in the standard resolvent and SPOD analysis captures near or more than 50% of the total energy. The first six modes are capable of recovering more than 85% of the small-scale energy, and more than 90% of the large-scale energy. This feature is not evident in the eddy-viscosity-improved resolvent analysis, with the first mode capturing only 2%–20% of the total energy, and the higher-order modes still holding significant energy. Nevertheless, such results do not reduce the accuracy of the response modes in the prediction of flow structures (Symon *et al.* 2023), since the singular value does not strictly convey the weight of the corresponding mode in recovering the flow field in resolvent analysis. The weight function is determined by both the singular value and the projection of the forcing mode on the real nonlinear process; see (14) in Fan *et al.* (2023).

Considering the representativeness of the first SPOD mode in terms of energy, we first examine its alignment with the optimal resolvent response mode with/without eddy viscosity. Figure 5 presents the wall-normal profiles of the streamwise velocity (\hat{u}_1), wall-normal velocity (\hat{u}_2), spanwise velocity (\hat{u}_3), density ($\hat{\rho}$) and temperature (\hat{T}) components of the optimal resolvent and the first SPOD mode at the representative scales

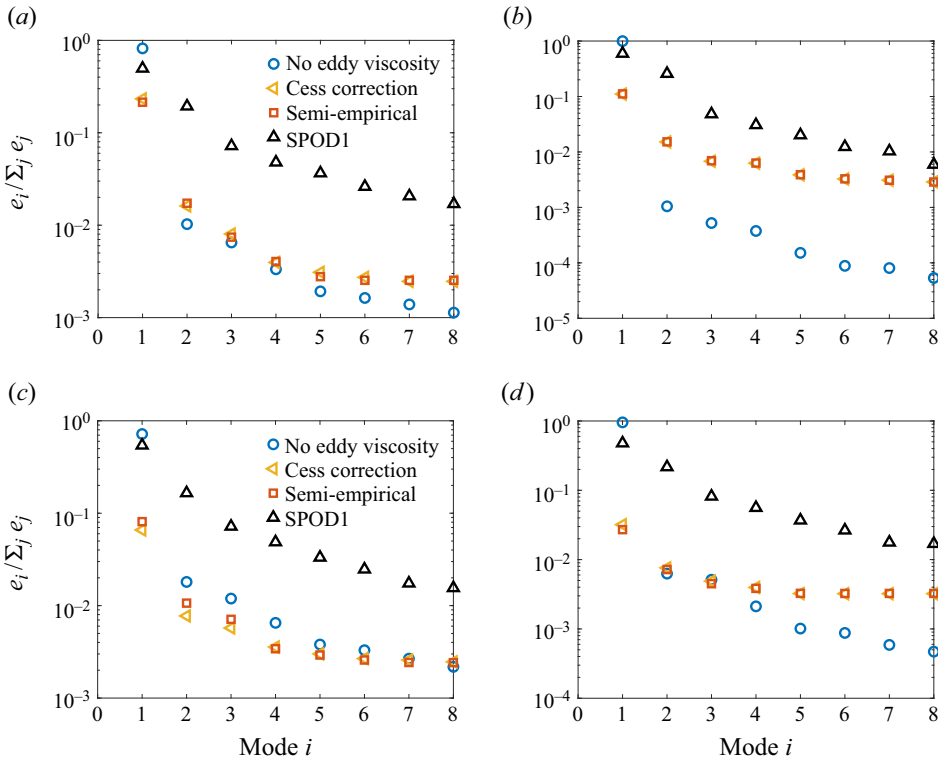


Figure 4. Energy contained in the i th resolvent and SPOD modes relative to the total, defined by $\sigma_i^2 / \sum_j \sigma_j^2$ and $\Lambda_i / \sum_j \Lambda_j$ (where Λ denotes the eigenvalue in the SPOD analysis), respectively, at (a) $(\lambda_1^+, \lambda_3^+, c) = (465, 96, 0.52)$ and (b) $(\lambda_1^+, \lambda_3^+, c) = (1210, 450, 0.89)$ in the adiabatic turbulent boundary layer, and (c) $(\lambda_1^+, \lambda_3^+, c) = (929, 208, 0.66)$ and (d) $(\lambda_1^+, \lambda_3^+, c) = (1239, 459, 0.88)$ in the cold-wall turbulent boundary layer.

in the adiabatic turbulent boundary layer. Generally, in figures 5(a–e), all three types of resolvent-based results are able to capture approximately the features in the distribution of perturbations, especially with respect to the correctly identified most energetic location following the critical-layer arguments (McKeon & Sharma 2010). More specifically, better agreements can be observed at the tails between the eddy-viscosity-improved resolvent and SPOD modes for all components, in contrast to the performance of the standard resolvent mode. It thus suggests a higher prediction accuracy of resolvent analysis with the addition of eddy viscosity in the near-wall cycle. The profiles with the addition of the Cess-correction and semi-empirical models are almost collapsed onto each other. A further comparison of the two eddy-viscosity models is performed, in terms of the mode shapes of the streamwise velocity. Details are shown in the Appendix. The remarkable consistency between the two models confirms that the optimal resolvent mode is not sensitive to the small differences in the eddy-viscosity quantities, as long as the μ_i model can resemble its real distribution appropriately (Cossu, Pujals & Depardon 2009).

For the larger energetic scales in the outer region, e.g. $(\lambda_1^+, \lambda_3^+, c) = (1210, 450, 0.89)$ in figures 5(f–j), the resolvent modes without eddy viscosity are localized narrowly, since they neglect the true nonlinear transfer of energy, hence the local production is dissipated rapidly by molecular viscosity. On the other hand, the predictive performances

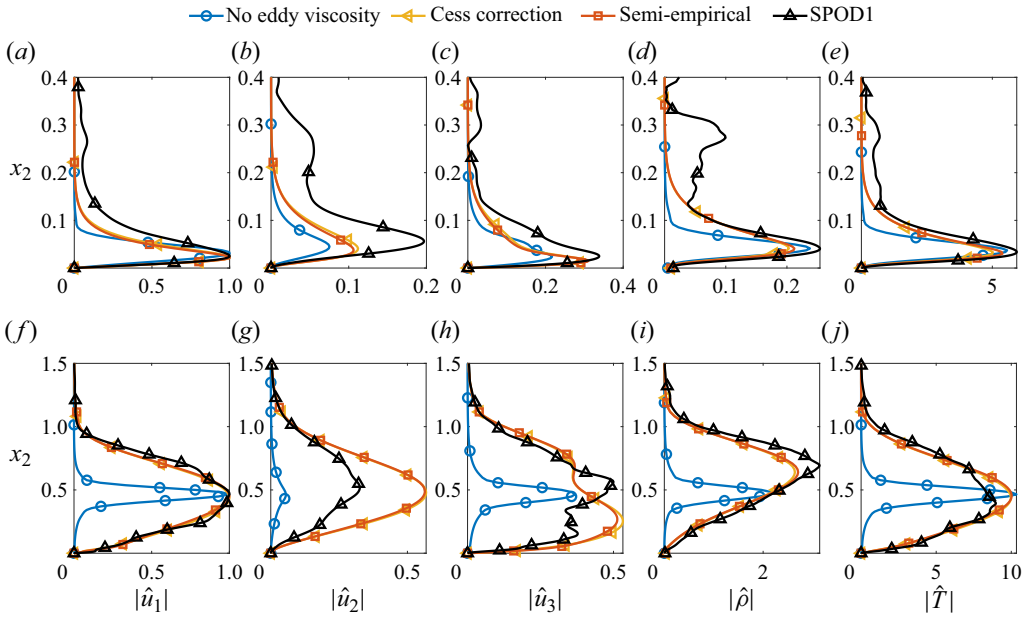


Figure 5. The streamwise velocity, wall-normal velocity, spanwise velocity, density and temperature components of the optimal resolvent with/without adding the semi-empirical eddy viscosity model and the leading SPOD mode at (a–e) $(\lambda_1^+, \lambda_3^+, c) = (465, 96, 0.52)$ and (f–j) $(\lambda_1^+, \lambda_3^+, c) = (1210, 450, 0.89)$, in the adiabatic turbulent boundary layer.

of the proposed eddy-viscosity-improved resolvent analysis are nearly perfect for the components \hat{u}_1 , $\hat{\rho}$ and \hat{T} , by modulating the energy transfer mechanism upon adding the eddy viscous work (Symon *et al.* 2021). As for the components \hat{u}_2 and \hat{u}_3 (in figures 5g,h), the resolvent-based predictions are degraded when compared with the SPOD profiles. Underestimations of these components are observed without eddy viscosity, which is associated with the nature of high non-normality in the shear flow operator (Symon *et al.* 2023). The addition of either eddy-viscosity profile is able to reduce the deviation between the resolvent and SPOD modes to some extent, exhibiting larger values of $|\hat{u}_2|$, $|\hat{u}_3|$ and $|\hat{\rho}|$ than the mode without eddy viscosity.

In the cold-wall case, a similar phenomenon is seen in figure 6. The addition of eddy viscosity makes the response modes richer in light of the wide spanning in the wall-normal direction, as mentioned earlier. Hence it provides a more efficient basis for turbulence prediction. In particular for the prediction of density and temperature perturbations close to the wall (in figures 6d,e), the inherent dual-peak feature is identified reasonably well in all types of resolvent modes, though no significant improvement is observed in the resolvent analysis with eddy viscosity. The dual-peak feature is ascribed to the non-monotonous profile of the mean temperature in the cold-wall turbulent boundary layer. The sign change in the mean temperature gradient leads to a reversed conductive and turbulent heat transfer in the wall-normal direction, which challenges the basic assumptions in the streamwise-velocity–temperature correlation (Wenzel, Gibis & Kloker 2022) and makes the prediction of the thermal statistics more difficult.

To assess quantitatively the alignment between the resolvent and SPOD modes, a coefficient β_{11} , which is defined by the projection of the optimal resolvent mode (ψ_1 or $\psi_{e,1}$) onto the first SPOD mode (\hat{q}_{SPOD1}) at each wavenumber combination, is introduced.

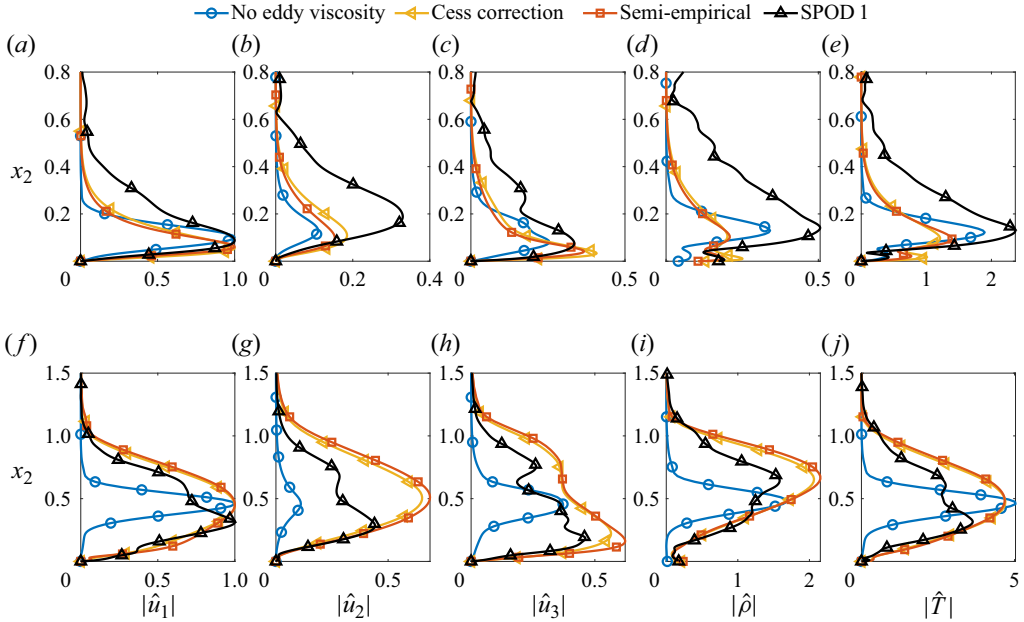


Figure 6. The streamwise velocity, wall-normal velocity, spanwise velocity, density and temperature components of the optimal resolution with/without adding the semi-empirical eddy viscosity model and the leading SPOD mode at (a–e) $(\lambda_1^+, \lambda_3^+, c) = (929, 208, 0.66)$ and (f–j) $(\lambda_1^+, \lambda_3^+, c) = (1239, 459, 0.88)$, in the cold-wall turbulent boundary layer.

It is written as

$$\beta_{11}(\kappa_1, \kappa_3, \omega) = \frac{\langle \hat{q}_{SPOD1}(x_2; \kappa_1, \kappa_3, \omega), \psi_1(x_2; \kappa_1, \kappa_3, \omega) \rangle}{\|\hat{q}_{SPOD1}(x_2; \kappa_1, \kappa_3, \omega)\| \times \|\psi_1(x_2; \kappa_1, \kappa_3, \omega)\|}, \quad (3.1)$$

where $\langle \cdot, \cdot \rangle$ denotes the inner product defined by Chu (1965), and $\|\cdot\|$ represents the weighted L_2 norm. Note that ψ_1 is replaced by $\psi_{e,1}$ when taking into account the eddy viscosity. Having $\beta_{11} = 1$ indicates perfect agreement between the two, giving identical identifications of turbulent structures and energy distribution, whereas $\beta_{11} = 0$ suggests that the SPOD mode and the resolvent mode are orthogonal to each other (Abreu *et al.* 2020; Pickering *et al.* 2021). For the scales under scrutiny in figures 5 and 6, the projection coefficient β_{11} is calculated and listed in table 1. Remarkable improvement of the representativeness of the optimal resolvent mode is seen clearly, especially for the larger scale where the added eddy viscosity plays a significant role in modelling the nonlinear energy transfer.

To examine the alignment at other scales, we sample at varying spanwise wavelengths and a fixed streamwise wavelength and wave speed, which is cross-sectional in the near-wall and outer-layer cycle, i.e. $(\lambda_1^+, c) = (430, 0.57)$ and $(\lambda_1^+, c) = (1291, 0.8)$ for the adiabatic case, and $(\lambda_1^+, c) = (929, 0.66)$ and $(\lambda_1^+, c) = (1239, 0.88)$ for the cold-wall case. The variation of β_{11} as a function of λ_3^+ is shown in figures 7 and 8. The background colour represents the turbulent energy spectra at the corresponding wall-normal location in the sense of the critical layer. As anticipated, for the near-wall scales shown in figures 7(a) and 8(a), β_{11} is larger than or close to 0.8 in the high-energy-containing region (e.g. $20 < \lambda_3^+ < 175$ in the adiabatic case, and $60 < \lambda_3^+ < 400$ in the cold-wall case), between either type of resolvent and SPOD modes. Only small variations are induced

Mode	Adiabatic case		Cold-wall case	
	$(\lambda_1^+, \lambda_3^+) = (465, 96),$ $c = 0.52$	$(\lambda_1^+, \lambda_3^+) = (1210, 450),$ $c = 0.89$	$(\lambda_1^+, \lambda_3^+) = (929, 208),$ $c = 0.66$	$(\lambda_1^+, \lambda_3^+) = (1239, 459),$ $c = 0.88$
No eddy viscosity	0.812	0.416	0.750	0.515
Cess-correction model	0.937	0.956	0.865	0.909
Semi-empirical model	0.930	0.956	0.850	0.905

Table 1. The alignment between the optimal resolvent and the first SPOD mode at two selected scales.

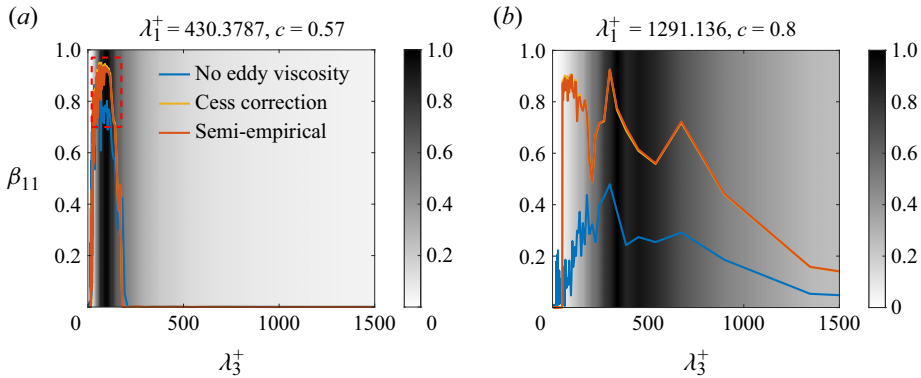


Figure 7. Variation of β_{11} with regard to the spanwise wavelength, in the adiabatic turbulent boundary layer. The background colour represents the normalized energy spectra at matching streamwise wavelengths and wall-normal locations.

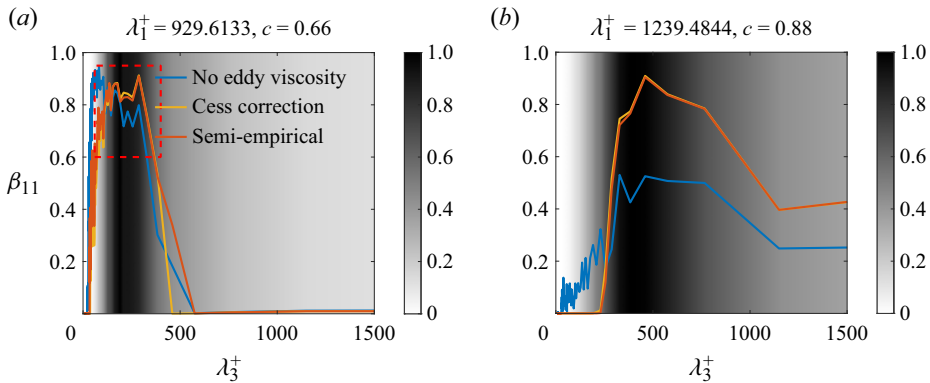


Figure 8. Variation of β_{11} with regard to the spanwise wavelength, in the cold-wall turbulent boundary layer.

by the addition of eddy viscosity. As highlighted by the red dashed box, the so-called ‘high-energy-containing region’ covers more than 70 % of the total energy at respective heights. Beyond this region, the value of β_{11} reduces dramatically, thus indicating a poor prediction of the low-energy-containing structures. Nonetheless, this biased predictive capability is believed to have limited impacts on constructing the full flow field, as the contribution of low-energy-containing structures is minor with low energy amplification.

To be more specific, we quantify the energy captured by the resolvent mode in contrast to that contained in the first SPOD mode ($E_{qq,SPOD1}$) at the characteristic wall-normal location, as shown in figure 9. The $E_{qq,SPOD1}$ value is calculated based on the energy spectra at matching streamwise wavelengths and wall-normal locations, which are obtained from DNS, premultiplied by the rate of the first eigenvalue to the total (i.e. $\Lambda_1 / \sum_j \Lambda_j$). In the adiabatic case, the energy distribution exhibited by the eddy-viscosity-improved resolvent mode aligns quite well with that of the first SPOD mode, especially in the highlighted ‘high-energy-containing region’. In general, both types of eddy-viscosity-improved modes are able to capture up to 53 % of the SPOD energy when integrated in the spanwise wavenumber direction, while the standard resolvent mode captures approximately 38 %. The situation is similar in the cold-wall turbulent boundary layer, with approximately 50 % of the energy captured in the resolvent mode with eddy viscosity, while 45 % is captured in the standard resolvent mode.

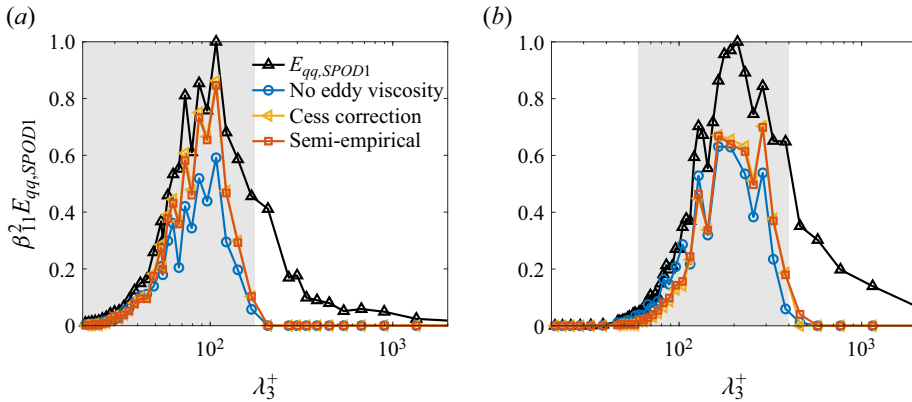


Figure 9. Energy distribution in the optimal resolvent modes and the first SPOD mode, for the near-wall cycle in the (a) adiabatic and (b) cold-wall turbulent boundary layers. The grey background covers the high-energy-containing region.

As for the energetic large-scale motions characterizing the outer-layer dynamics in figures 7(b) and 8(b), although the general performance is poorer than that for the small scales, the addition of the proposed eddy-viscosity model indeed enhances the projection coefficients. Hence it confirms the efficient role of the rational eddy-viscosity models in resolvent-based reduced-order modelling.

In addition to the wall-normal profiles of the state variables, the distribution of the cross-spectral density (CSD) is of great concern in turbulence prediction, since it can properly reconstruct the second-order statistics of the flow (Towne *et al.* 2018). The low-rank approximation of the CSD tensor is calculated by the optimal response mode at a particular wavenumber pair:

$$S_{11}(x_2, x'_2; \kappa_1, \kappa_3, \omega) = \hat{\psi}_1(x_2; \kappa_1, \kappa_3, \omega) \hat{\psi}_1^\dagger(x'_2; \kappa_1, \kappa_3, \omega). \quad (3.2)$$

The absolute value of the modelled rank-1 CSD for each component (including \hat{u}_1 , \hat{u}_2 , \hat{u}_3 , $\hat{\rho}$ and \hat{T}) is plotted as a function of x_2 and x'_2 in figure 10, at the two selected scales in the adiabatic turbulent boundary layer. At small scales (figure 10a), the three types of resolvent-based models are expected to reproduce faithfully the CSD from SPOD results. A slight exception occurs in the autocorrelation and cross-correlations of \hat{u}_3 . As we see in the third row and the third column, the μ_r -modelled energy densities appear at a lower height. This indicates that the addition of eddy viscosity introduces a strong energy transfer among components near the wall, since the spanwise velocity receives energy from the streamwise and wall-normal components, due to the effect of pressure strain and splat (Lee & Moser 2019; Fan *et al.* 2022). Moreover, the additional eddy diffusion also plays a critical role in the positive energy receipt in the near-wall region (Symon *et al.* 2023). At a larger energetic scale (figure 10b), the CSD results using the Cess-correction and semi-empirical models are also observed to be very similar to each other, and they exhibit much better alignment with the DNS data in contrast to those without an eddy-viscosity model. A very narrow distribution is observed in the CSD without eddy viscosity, and the turbulent energy decays from its peak dramatically, consistent with the observations in the profiles of the response mode. This issue can be alleviated efficiently with the addition of eddy viscosity, suggesting that the eddy-viscosity models help to improve the mode representation of the second-order turbulent statistics. Hence the influence of the dominant

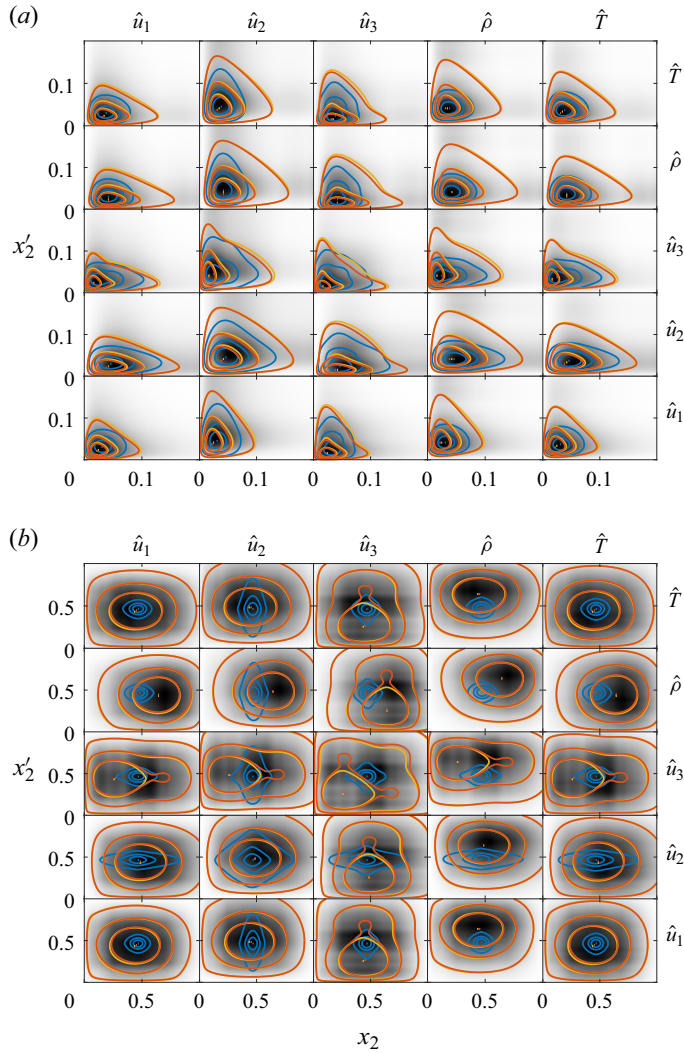


Figure 10. Absolute value of the CSD for each component, at (a) $(\lambda_1^+, \lambda_3^+, c) = (465, 96, 0.52)$ and (b) $(\lambda_1^+, \lambda_3^+, c) = (1210, 450, 0.89)$, in the adiabatic turbulent boundary layer. The background colour represents the CSD of the first SPOD results. The contour lines indicate 0.3, 0.6 and 0.9 of their respective maximum, moving inwards, and the legend for the coloured lines is as in [figure 7](#).

turbulent structures can be identified more accurately in the eddy-viscosity-improved resolvent analysis.

For the CSD prediction in the cold-wall cases, as shown in [figure 11](#), the situation is similar. The predictive performance is greatly improved by using the eddy-viscosity-improved resolvent analysis. Therefore, the reliability and improvement of the proposed models in comparison with the standard resolvent-based modelling, for the prediction of turbulent fluctuations in the compressible turbulent boundary layers, are believed to be achieved.

At last, although the first (optimal) mode is believed to be of the greatest importance in terms of energy occupation, the alignment of the other resolvent and SPOD modes is also of interest. We project the first four response modes onto the corresponding SPOD

Eddy-viscosity-improved resolvent analysis

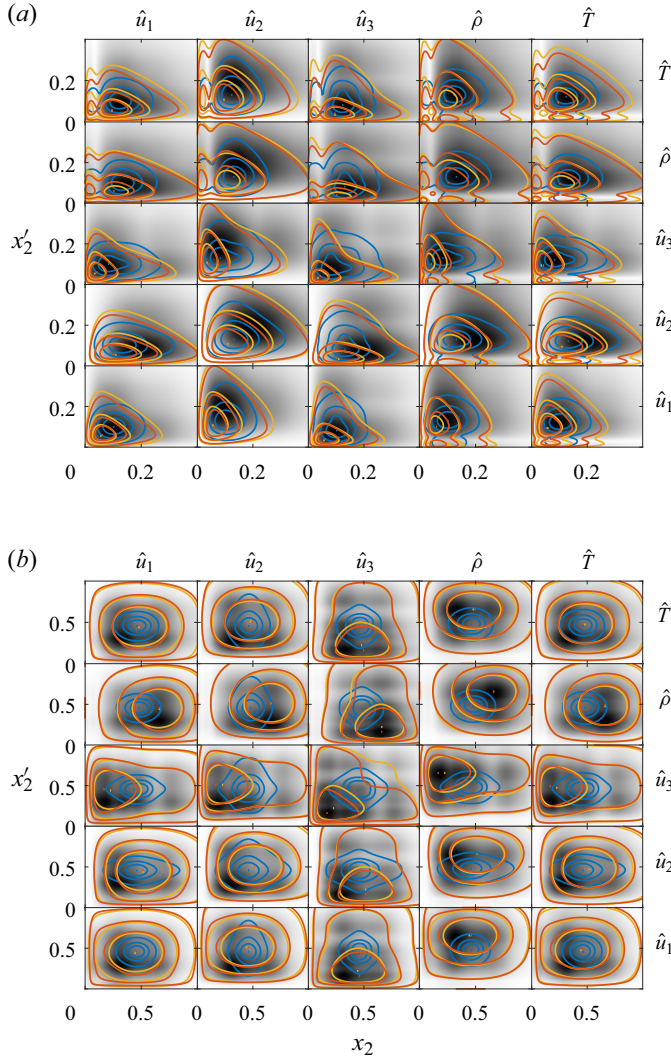


Figure 11. Absolute value of the CSD for each component, at (a) $(\lambda_1^+, \lambda_3^+, c) = (929, 208, 0.66)$ and (b) $(\lambda_1^+, \lambda_3^+, c) = (1239, 459, 0.88)$, in the cold-wall turbulent boundary layer.

modes, and the projection coefficients are shown in figures 12 and 13 for the adiabatic and cold-wall turbulent boundary layers, respectively. The projection coefficient is formulated as

$$\beta_{ij}(\kappa_1, \kappa_3, \omega) = \frac{|\langle \hat{q}_{SPODi}(x_2; \kappa_1, \kappa_3, \omega), \psi_j(x_2; \kappa_1, \kappa_3, \omega) \rangle|}{\|\hat{q}_{SPODi}(x_2; \kappa_1, \kappa_3, \omega)\| \times \|\psi_j(x_2; \kappa_1, \kappa_3, \omega)\|}, \quad (3.3)$$

where \hat{q}_{SPODi} denotes the i th SPOD mode. For the near-wall cycle in both cases, evident promotion of the eddy-viscosity models is observed only in some of the modes, e.g. the first and third resolvent modes at the scale under scrutiny. Similarities between the two proposed eddy-viscosity-improved resolvent analyses are also observed in higher-order modes. On the other hand, for the larger scales in the outer region, the plots in figures 12(d–f) and 13(d–f) show that the projection coefficients of the

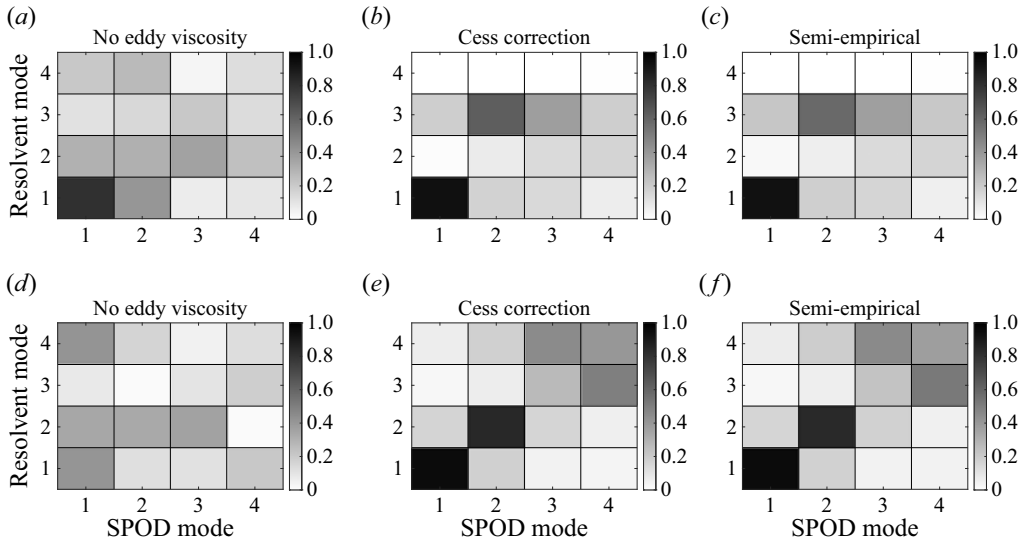


Figure 12. Projections of the first four response modes onto the corresponding SPOD modes, at (a–c) $(\lambda_1^+, \lambda_3^+, c) = (465, 96, 0.52)$ and (d–f) $(\lambda_1^+, \lambda_3^+, c) = (1210, 450, 0.89)$, in the adiabatic turbulent boundary layer.

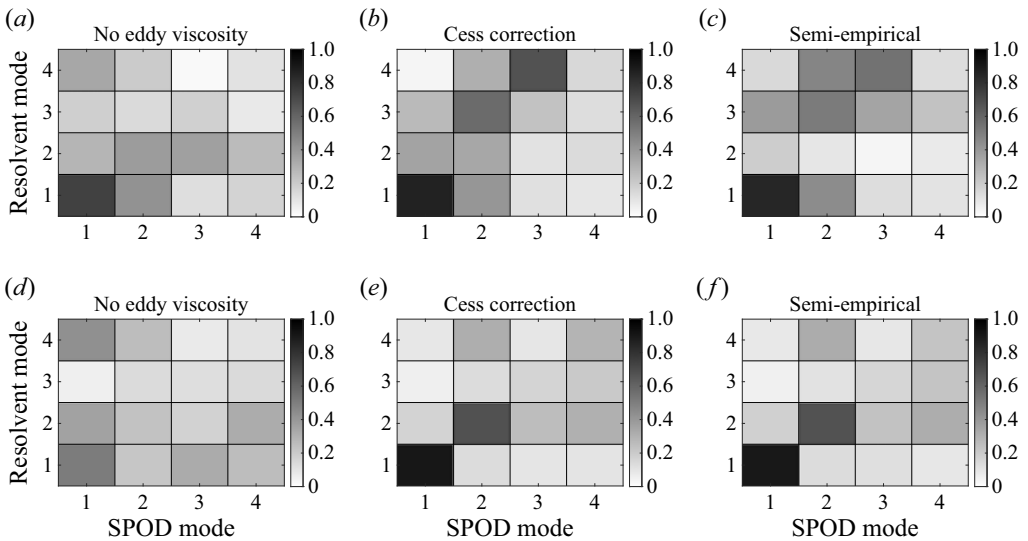


Figure 13. Projections of the first four response modes onto the corresponding SPOD modes, at (a–c) $(\lambda_1^+, \lambda_3^+, c) = (929, 208, 0.66)$ and (d–f) $(\lambda_1^+, \lambda_3^+, c) = (1239, 459, 0.88)$, in the cold-wall turbulent boundary layer.

eddy-viscosity-improved modes at the diagonal line (i.e. β_{ii}) are all superior to those of the standard modes. Hence in these cases, higher-order resolvent modes can help to improve the capability of turbulence modelling/prediction, in particular in that the second SPOD modes capture more than 20% of the total energy for large-scale motions (see figures 4b,d).

4. Summary





This paper develops two eddy-viscosity models to improve the low-rank approximation of resolvent analysis in compressible turbulent boundary layers, i.e. a modified Cess eddy-viscosity model and a new semi-empirical eddy-viscosity model. The models are represented with a two-layer algebraic expression, considering the composite-layer nature of the turbulent boundary layer. The first model is a correction of the classical Cess model, based on the compressibility transformation in the inner region and the mixing-length hypothesis in the outer region, such that the density variation and the outer-layer difference between the boundary layer and the channel flow are properly modelled. Considering the exclusive features of zero-pressure-gradient turbulent boundary layers, the second model is proposed based on an empirical fitting law of the total shear stress and the mixing-length theory.

In the *a priori* tests, both models are able to capture the tendency of the eddy-viscosity profile reasonably well; nonetheless, the semi-empirical model seems to outperform the corrected Cess model. With the DNS data of two hypersonic turbulent boundary layers, comparisons between the resolvent response modes with/without eddy viscosity and the SPOD modes are conducted in terms of the perturbations of velocities, density and temperature. Results show that the predictive performance of the optimal resolvent mode in turbulent motions is improved significantly by adding eddy viscosity in the resolvent operator, especially at the high-energy-containing scales, confirming the promising low-rank approximations of resolvent analysis with the proposed eddy-viscosity models. It is also noted that there is no significant difference observed between the predictions with the two models, suggesting that the optimal response mode is not sensitive to the relatively small differences in the eddy-viscosity quantities, as long as its distribution can be represented properly.

Funding. Funding support from the National Natural Science Foundation of China (under grant no. 12372221) is acknowledged. The authors also acknowledge support from the joint PhD framework (programme) of Shanghai Jiao Tong University and the University of Melbourne.

Declaration of interests. The authors report no conflict of interest.

Author ORCIDs.

-  Yitong Fan <https://orcid.org/0000-0001-8583-9670>;
-  Melissa Kozul <https://orcid.org/0000-0001-9881-1677>;
-  Weipeng Li <https://orcid.org/0000-0002-0335-4934>;
-  Richard D. Sandberg <https://orcid.org/0000-0001-5199-3944>.

Appendix. Resolvent mode shapes of the streamwise velocity

Figure 14 shows the mode shapes of the streamwise velocity in the wall-normal–temporal (x_2-t) plane, using SPOD analysis and resolvent analysis with/without the addition of eddy-viscosity models, in the adiabatic turbulent boundary layer. Common features are observed in all types of modes: the shapes are all inclined, exhibiting a phase variation in both the wall-normal and temporal directions. The positive and negative values appear alternatively along the t direction. In contrast to the response in figure 14(b), the eddy-viscosity-improved modes are more outstretched in the wall-normal coordinate, containing richer flow information, which is more similar to the SPOD mode in figure 14(a). In this sense, the eddy-viscosity-improved modes provide a more promising basis for predicting the turbulent structures, which agrees well with the aforementioned discussion. As for the comparison between the two eddy-viscosity models, a high degree

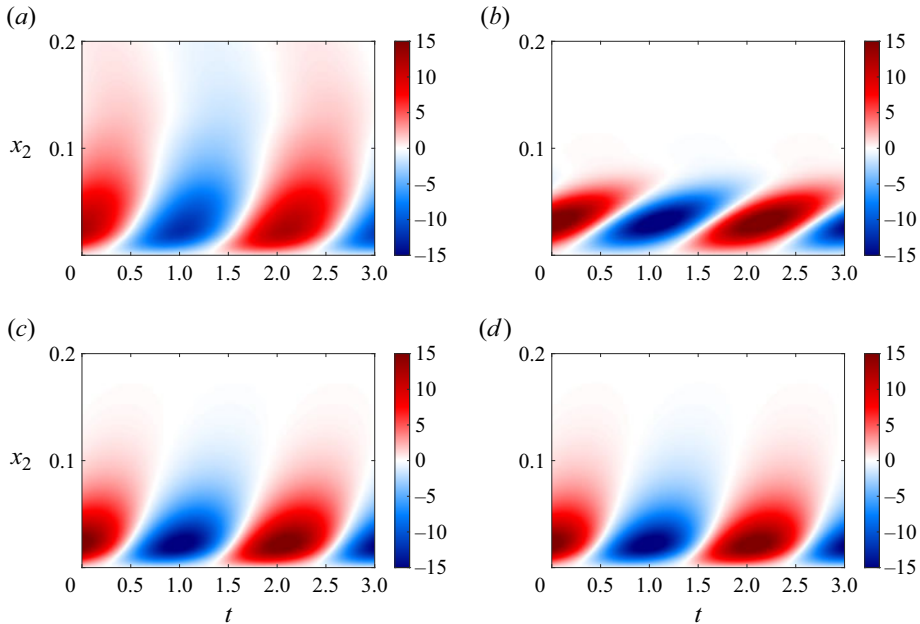


Figure 14. Mode shapes of the streamwise velocity in the wall-normal–temporal plane, using (a) SPOD analysis and (b–d) resolvent analysis, with (b) no eddy viscosity, (c) the Cess-correction model and (d) the semi-empirical model, at $(\lambda_1^+, \lambda_3^+, c) = (465, 96, 0.52)$ in the adiabatic turbulent boundary layer.

of consistency is observed in the shape contours in figures 14(c,d). Hence this further confirms that the resolvent analysis is insensitive to the small variations of eddy-viscosity quantities. At more scales in adiabatic and cold-wall turbulent boundary layers, similar features are observed, thus the plots are not shown here.

REFERENCES

- ABREU, L.I., CAVALIERI, A.V.G., SCHLATTER, P., VINUESA, R. & HENNINGSON, D.S. 2020 Resolvent modelling of near-wall coherent structures in turbulent channel flow. *Intl J. Heat Fluid Flow* **85**, 108662.
- AMARAL, F.R., CAVALIERI, A.V.G., MARTINI, E., JORDAN, P. & TOWNE, A. 2021 Resolvent-based estimation of turbulent channel flow using wall measurements. *J. Fluid Mech.* **927**, A17.
- BAE, H.J., DAWSON, S.T.M. & MCKEON, B.J. 2020a Resolvent-based study of compressibility effects on supersonic turbulent boundary layers. *J. Fluid Mech.* **883**, A29.
- BAE, H.J., DAWSON, S.T.M. & MCKEON, B.J. 2020b Studying the effect of wall cooling in supersonic boundary layer flow using resolvent analysis. *AIAA Scitech 2020 Forum*. AIAA.
- BERKOOZ, G., HOLMES, P. & LUMLEY, J.L. 1993 The proper orthogonal decomposition in the analysis of turbulent flows. *Annu. Rev. Fluid Mech.* **25** (1), 539–575.
- BERNARDINI, M. & PIROZZOLI, S. 2011 Wall pressure fluctuations beneath supersonic turbulent boundary layers. *Phys. Fluids* **23** (8), 085102.
- CEBECI, T. 1971 Calculation of compressible turbulent boundary layers with heat and mass transfer. *AIAA J.* **9** (6), 1091–1097.
- CEBECI, T. 2004 4 – general behavior of turbulent boundary layers. In *Analysis of Turbulent Flows* (ed. T. Cebeci), pp. 81–140. Elsevier.
- CESS, R.D. 1958 A survey of the literature on heat transfer in turbulent tube flow. *Tech. Rep.* 8-0529-R24. Westinghouse Research.
- CHEN, X.-L., CHENG, C., FU, L. & GAN, J.-P. 2023 Linear response analysis of supersonic turbulent channel flows with a large parameter space. *J. Fluid Mech.* **962**, A7.
- CHU, B.-T. 1965 On the energy transfer to small disturbances in fluid flow (Part I). *Acta Mechanica* **1** (3), 215–234.

- COSSU, C., PUJALS, G. & DEPARDON, S. 2009 Optimal transient growth and very large-scale structures in turbulent boundary layers. *J. Fluid Mech.* **619**, 79–94.
- DAWSON, S.T.M. & MCKEON, B.J. 2019 Studying the effects of compressibility in planar Couette flow using resolvent analysis. *AIAA Scitech 2019 Forum. San Diego, California*. AIAA.
- DAWSON, S.T.M., MCKEON, B.J. & SAXTON-FOX, T. 2018 Modeling passive scalar dynamics in wall-bounded turbulence using resolvent analysis. In 2018 *Fluid Dynamics Conference. Atlanta, Georgia*. AIAA.
- VAN DRIEST, E.R. 1951 Turbulent boundary layer in compressible fluids. *J. Aeronaut. Sci.* **18** (3), 145–160.
- ESCUDIER, M.P. 1966 The distribution of mixing length in turbulent flows near walls. *Tech. Rep.* Heat Transfer Section TWF/TN/12. Imperial College London.
- FAN, Y.-T. & LI, W.-P. 2023 Spectral analysis of turbulence kinetic and internal energy budgets in hypersonic turbulent boundary layers. *Phys. Rev. Fluids* **8**, 044604.
- FAN, Y.-T., LI, W.-P. & PIROZZOLI, S. 2022 Energy exchanges in hypersonic flows. *Phys. Rev. Fluids* **7**, L092601.
- FAN, Y.-T., LI, W.-P. & SANDBERG, R.D. 2023 Resolvent-based analysis of hypersonic turbulent boundary layers with/without wall cooling. *Phys. Fluids* **35** (4), 045118.
- GUPTA, V., MADHUSUDANAN, A., WAN, M.-P., ILLINGWORTH, S.J. & JUNIPER, M.P. 2021 Linear-model-based estimation in wall turbulence: improved stochastic forcing and eddy viscosity terms. *J. Fluid Mech.* **925**, A18.
- HE, W. & TIMME, S. 2020 Resolvent analysis of shock buffet on infinite wings. *AIAA Paper 2020–2727*.
- HOLFORD, J.J., LEE, M. & HWANG, Y. 2023 Optimal white-noise stochastic forcing for linear models of turbulent channel flow. *J. Fluid Mech.* **961**, A32.
- HOU, Y., SOMANDEPALLI, V.S.R. & MUNGAL, M.G. 2006 A technique to determine total shear stress and polymer stress profiles in drag reduced boundary layer flows. *Exp. Fluids* **40**, 589–600.
- ILLINGWORTH, S.J., MONTY, J.P. & MARUSIC, I. 2018 Estimating large-scale structures in wall turbulence using linear models. *J. Fluid Mech.* **842**, 146–162.
- JIN, B., ILLINGWORTH, S.J. & SANDBERG, R.D. 2022 Resolvent-based approach for H_2 -optimal estimation and control: an application to the cylinder flow. *Theor. Comput. Fluid Dyn.* **36**, 491–515.
- JIN, B., SYMON, S. & ILLINGWORTH, S.J. 2021 Energy transfer mechanisms and resolvent analysis in the cylinder wake. *Phys. Rev. Fluids* **6** (2), 024702.
- JOVANOVIĆ, M.R. 2021 From bypass transition to flow control and data-driven turbulence modeling: an input–output viewpoint. *Annu. Rev. Fluid Mech.* **53** (1), 311–345.
- KARBAN, U., MARTINI, E., CAVALIERI, A.V.G., LESSHAFFT, L. & JORDAN, P. 2022 Self-similar mechanisms in wall turbulence studied using resolvent analysis. *J. Fluid Mech.* **939**, A36.
- KOJIMA, Y., YEH, C.-A., TAIRA, K. & KAMEDA, M. 2020 Resolvent analysis on the origin of two-dimensional transonic buffet. *J. Fluid Mech.* **885**, R1.
- LEE, M.-K. & MOSER, R.D. 2019 Spectral analysis of the budget equation in turbulent channel flows at high Reynolds number. *J. Fluid Mech.* **860**, 886–938.
- LESSHAFFT, L., SEMERARO, O., JAUNET, V., CAVALIERI, A.V.G. & JORDAN, P. 2019 Resolvent-based modeling of coherent wave packets in a turbulent jet. *Phys. Rev. Fluids* **4**, 063901.
- LUMLEY, J.L. 1967 The structure of inhomogeneous turbulent flows. In *Atmospheric Turbulence and Radio Wave Propagation* (ed. A.M. Yaglom & V.I. Tartarsky), pp. 166–177. Nauka.
- MACK, L.M. 1984 Boundary-layer linear stability theory. *Tech. Rep.* AGARD Report No. 709. NASA Jet Propulsion Laboratory.
- MADHUSUDANAN, A., ILLINGWORTH, S.J. & MARUSIC, I. 2019 Coherent large-scale structures from the linearized Navier–Stokes equations. *J. Fluid Mech.* **873**, 89–109.
- MADHUSUDANAN, A. & MCKEON, B.J. 2022 Subsonic and supersonic mechanisms in compressible turbulent boundary layers: a perspective from resolvent analysis. [arXiv:2209.14223](https://arxiv.org/abs/2209.14223).
- MARTINI, E., CAVALIERI, A.V.G., JORDAN, P., TOWNE, A. & LESSHAFFT, L. 2020 Resolvent-based optimal estimation of transitional and turbulent flows. *J. Fluid Mech.* **900**, A2.
- MARTINI, E., JUNG, J., CAVALIERI, A.V.G., JORDAN, P. & TOWNE, A. 2022 Resolvent-based tools for optimal estimation and control via the Wiener–Hopf formalism. *J. Fluid Mech.* **937**, A19.
- MCKEON, B.J. 2017 The engine behind (wall) turbulence: perspectives on scale interactions. *J. Fluid Mech.* **817**, P1.
- MCKEON, B.J. & SHARMA, A.S. 2010 A critical-layer framework for turbulent pipe flow. *J. Fluid Mech.* **658**, 336–382.
- MOARREF, R., JOVANOVIĆ, M.R., TROPP, J.A., SHARMA, A.S. & MCKEON, B.J. 2014 A low-order decomposition of turbulent channel flow via resolvent analysis and convex optimization. *Phys. Fluids* **26** (5), 051701.

- MOARREF, R., SHARMA, A.S., TROPP, J.A. & MCKEON, B.J. 2013a Model-based scaling of the streamwise energy density in high-Reynolds-number turbulent channels. *J. Fluid Mech.* **734**, 275–316.
- MOARREF, R., SHARMA, A.S., TROPP, J.A. & MCKEON, B.J. 2013b On effectiveness of a rank-1 model of turbulent channels for representing the velocity spectra. In *43rd Fluid Dynamics Conference*. AIAA.
- MORRA, P., NOGUEIRA, P.A.S., CAVALIERI, A.V.G. & HENNINGSON, D.S. 2021 The colour of forcing statistics in resolvent analyses of turbulent channel flows. *J. Fluid Mech.* **907**, A24.
- MORRA, P., SEMERARO, O., HENNINGSON, D.S. & COSSU, C. 2019 On the relevance of Reynolds stresses in resolvent analyses of turbulent wall-bounded flows. *J. Fluid Mech.* **867**, 969–984.
- PICKERING, E., RIGAS, G., SCHMIDT, O.T., SIPP, D. & COLONIUS, T. 2021 Optimal eddy viscosity for resolvent-based models of coherent structures in turbulent jets. *J. Fluid Mech.* **917**, A29.
- PIROZZOLI, S. & BERNARDINI, M. 2011 Turbulence in supersonic boundary layers at moderate Reynolds number. *J. Fluid Mech.* **688**, 120–168.
- POPE, S.B. 2000 *Turbulent Flows*. Cambridge University Press.
- PUJALS, G., GARCÍA-VILLALBA, M., COSSU, C. & DEPARDON, S. 2009 A note on optimal transient growth in turbulent channel flows. *Phys. Fluids* **21** (1), 015109.
- REYNOLDS, W.C. & HUSSAIN, A.K.M.F. 1972 The mechanics of an organized wave in turbulent shear flow. Part 3. Theoretical models and comparisons with experiments. *J. Fluid Mech.* **54** (2), 263–288.
- SCHMIDT, O.T., TOWNE, A., RIGAS, G., COLONIUS, T. & BRÈS, G.A. 2018 Spectral analysis of jet turbulence. *J. Fluid Mech.* **855**, 953–982.
- SHARMA, A.S. & MCKEON, B.J. 2013 On coherent structure in wall turbulence. *J. Fluid Mech.* **728**, 196–238.
- SYMON, S., ILLINGWORTH, S.J. & MARUSIC, I. 2020 Large-scale structures predicted by linear models of wall-bounded turbulence. *J. Phys.: Conf. Ser.* **1522** (1), 012006.
- SYMON, S., ILLINGWORTH, S.J. & MARUSIC, I. 2021 Energy transfer in turbulent channel flows and implications for resolvent modelling. *J. Fluid Mech.* **911**, A3.
- SYMON, S., MADHUSUDANAN, A., ILLINGWORTH, S.J. & MARUSIC, I. 2023 Use of eddy viscosity in resolvent analysis of turbulent channel flow. *Phys. Rev. Fluids* **8**, 064601.
- TAIRA, K., BRUNTON, S.L., DAWSON, S.T.M., ROWLEY, C.W., COLONIUS, T., MCKEON, B.J., SCHMIDT, O.T., GORDEYEV, S., THEOFILIS, V. & UKEILEY, L.S. 2017 Modal analysis of fluid flows: an overview. *AIAA J.* **55** (12), 4013–4041.
- TOWNE, A., SCHMIDT, O.T. & COLONIUS, T. 2018 Spectral proper orthogonal decomposition and its relationship to dynamic mode decomposition and resolvent analysis. *J. Fluid Mech.* **847**, 821–867.
- WENZEL, C., GIBIS, T. & KLOKER, M. 2022 About the influences of compressibility, heat transfer and pressure gradients in compressible turbulent boundary layers. *J. Fluid Mech.* **930**, A1.
- WU, T. & HE, G.-W. 2023 Composition of resolvents enhanced by random sweeping for large-scale structures in turbulent channel flows. *J. Fluid Mech.* **956**, A31.
- XIA, Z.-H., ZHANG, P. & YANG, X.I.A. 2021 On skin friction in wall-bounded turbulence. *Acta Mechanica Sin.* **37** (4), 589–598.
- ZARE, A., JOVANOVIĆ, M.R. & GEORGIU, T.T. 2017 Colour of turbulence. *J. Fluid Mech.* **812**, 636–680.
- ZHANG, C., DUAN, L. & CHOUDHARI, M.M. 2018 Direct numerical simulation database for supersonic and hypersonic turbulent boundary layers. *AIAA J.* **56** (11), 4297–4311.
- ZHANG, Y.-S., BI, W.-T., HUSSAIN, F. & SHE, Z.-S. 2014 A generalized Reynolds analogy for compressible wall-bounded turbulent flows. *J. Fluid Mech.* **739**, 392–420.